



Modeling of Fiber Optic Gold SPR Sensor Using Different Dielectric Function Models: A Comparative Study

Adel R. Sarhan¹ · Bedir Bedir Yousif^{2,3} · Nihal F. F. Areed² · Salah S. A. Obaya^{2,4}

Received: 9 November 2019 / Accepted: 4 May 2020 / Published online: 29 May 2020
© Springer Science+Business Media, LLC, part of Springer Nature 2020

Abstract

The performance of surface plasmon resonance (SPR) sensors has great dependence on its plasmonic material's frequency response, which is described by the complex dielectric function. Through history, researchers developed and enhanced mathematical models to accurately describe the material dielectric function. Although many papers compared the accuracy of different dielectric function models and stated its limitations, none of it addressed the effect of dielectric function model on the SPR sensor's characteristics. In this paper, we investigated the performance of the three most used dielectric function models (Drude, Lorentz-Drude, and Brendel-Bormann) and their effect on the theoretically obtained sensor parameters when used in a gold SPR sensor's model and validated it with the experimentally measured dielectric function. The result showed that using less accurate dielectric function's model has a drastic effect on the theoretically obtained sensor's parameters. Among the three models, the widely used Drude model was not the most accurate; alternatively, Brendel-Bormann model was the most accurate.

Keywords Surface plasmon resonance · Dielectric function · Fiber optic sensor · Drude · Lorentz · Brendel-Bormann

Introduction

Surface plasmon resonance occurs when a photon hits the interface between two materials with dielectric function of opposite signs (typically, a metal film and a dielectric). At a certain angle of incidence, electrons in the metal surface layer absorb a portion of the p-polarized incident light and oscillates in response to light excitation. These electron excitations are called plasmons. They propagate parallel to the metal surface generating a surface plasmon wave (SPW) in the interface. SPW frequency depends on the parameters of the sample

solution near the interface, namely, on the average refractive index near the sensor's surface [1–3].

Because of its prominent features such as its sensitivity, fast response, great accuracy, radio frequency interference (RFI), and electromagnetic interference (EMI) immunity and its relatively small size and low cost, surface plasmon resonance (SPR) sensors have been a major subject of interest during the last two decade [4, 5].

The first observed SPR phenomena were by Wood [6], but Liedberg et al. [7] introduced the principle for gas sensing and bio-sensing. Since then, a numerous SPR sensing structures have been reported. Many introduced different sensor configurations like removing the fiber cladding [8–10], tapering the fiber [11, 12], U-bent fiber [13–15], and the use of fiber Bragg grating [16–18].

On the other hand, investigating the optimal plasmonic materials was never settle, starting with metals gold [11, 14, 16–18], silver [9–11, 13], aluminum [19–21], copper [22, 23], and platinum [24, 25] to semiconductors [26, 27] and graphene [8, 13, 15, 16, 21, 23]. The plasmonic material performance depends on how it interacts with light: transmission, absorption, and reflection. This behavior is described by the material complex dielectric function [3]. The complex dielectric function consists of a real part and an imaginary part that describe the deflection of light and its absorption, respectively.

✉ Adel R. Sarhan
asarhan19@hotmail.com

Bedir Bedir Yousif
Bedir.yousif@gmail.com

¹ Electronics and Communications Department, Faculty of Engineering, Alexandria University, Alexandria, Egypt

² Electronics and Communications Department, Faculty of Engineering, Mansoura University, Mansoura, Egypt

³ Electronics and Communications Department, Faculty of Engineering, Kafrelsheikh University, Kafrelsheikh, Egypt

⁴ Zewail City of Science and Technology, Giza, Egypt

There are different calculation methods for determination of metal complex dielectric function (permittivity); the most common are Drude, Lorentz-Drude (L-D), and Brendel-Bormann (B-B). Drude model is the basic one, which describes the free electron effects and proves to be accurate for the low-energy part of the dielectric function [3, 28, 29]. Lorentz reduced the error in Drude model by adding a compensation term for the inter-band electron transitions. Although L-D model extends the validity of dielectric function calculation, it could not describe the sharp absorption, especially in noble metals [28]. The B-B model further improves the accuracy by replacing Lorentz oscillators with a superposition of infinite number of oscillators.

Many studies compared the three models' performance relevant to measured data; the B-B model showed the best accuracy with more than 94% overlap with the measured data; L-D model was less accurate, and Drude model was the least accurate [28–31]. Although the Drude model performance was not the best, many SPR sensor studies adopted it as a simple calculation method for metal complex dielectric function [32–35], and few papers used the more accurate L-D model [36, 37].

In this paper, we investigated how the selection of the used dielectric function model affects the gold SPR sensor's characteristics, mainly the sensitivity, full width at half maximum (FWHM), and the signal-to-noise ratio (SNR), using the three dielectric function models Drude, L-D, and B-B, and the experimentally measured dielectric function introduced in [38].

Method

We created a model of gold SPR fiber optic sensor; the sensor consisted of a fused silica multimode fiber with a part of its cladding removed and a thin layer of gold deposited on its core as shown in Fig. 1. The fiber optic parameters are shown in Table 1.

The fiber core refractive index has been calculated using Sellmeier formula Eq. (1) of fused silica dispersion in visible and near-infrared range [39]:

Table 1 Fiber optic parameters

Parameter	Value
Core diameter (D)	600 μm
Sensing area length (L)	15 mm
Numerical aperture (NA)	0.24
Gold layer depth (d)	50 nm

$$n_c^2(\lambda) = 1 + \sum_{i=1}^M \frac{B_i \lambda^2}{\lambda^2 - \lambda_i^2} \quad (1)$$

where B_i is the i^{th} oscillator strength for the resonance wavelength λ_i (Table 2) and λ indicates the wavelength of incident light in (μm).

Dielectric Function Models

We created three sensor models adopting each of Drude, L-D, and B-B models as the dielectric function's calculation model using parameters provided in [28] and another reference model using the experimentally measured data of the dielectric function obtained from [38].

Drude model:

$$\epsilon(\omega) = 1 - \frac{\Omega_p^2}{\omega(\omega - i\Gamma_0)} \quad (2)$$

Lorentz-Drude model:

$$\epsilon(\omega) = 1 - \frac{\Omega_p^2}{\omega(\omega - i\Gamma_0)} + \sum_{j=1}^k \frac{f_j \omega_p^2}{(\omega_j^2 - \omega^2) + i\omega\Gamma_j} \quad (3)$$

where ω_p is the plasma frequency, k is the number of oscillators with frequency ω_j , strength f_j , and lifetime $1/\Gamma_j$, while $\Omega_p = \sqrt{f_o} \omega_p$ is the plasma frequency associated with intraband transitions with oscillator strength f_o and damping constant Γ_o .

Fig. 1 Sensor's configuration

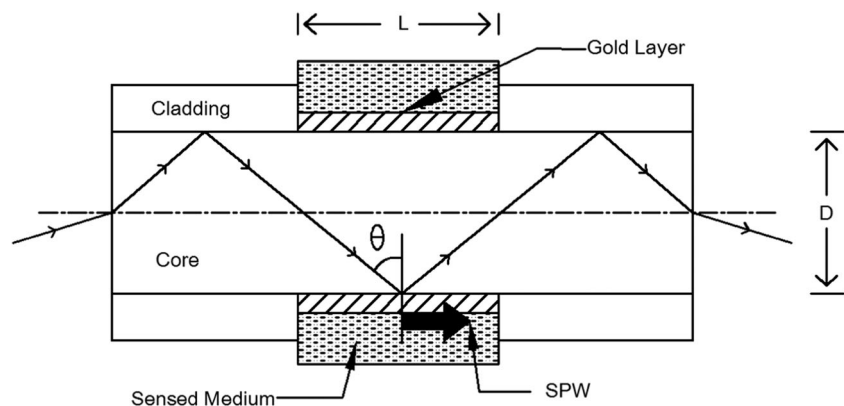


Table 2 Sellmeier constants for fused silica [39]

B1	0.6961663	λ_1	0.0684043
B2	0.4079426	λ_2	0.1162414
B3	0.8974794	λ_3	9.8961610

Brendel-Bormann model:

$$\epsilon(\omega) = 1 - \frac{\Omega_p^2}{\omega(\omega - i\Gamma_0)} + \sum_{j=1}^k \chi_j(\omega) \tag{4}$$

where

$$\chi_j(\omega) = \frac{1}{\sqrt{2\pi}\sigma_j} \int_{-\infty}^{\infty} \exp\left[-\frac{(x-\omega_j)^2}{2\sigma_j^2}\right] \times \frac{f_j\omega_p^2}{(x^2-\omega^2) + i\omega\Gamma_j} dx \tag{5}$$

Since the B-B model’s integral calculation solution contains the computation of the complex complementary error

function: $\text{erfc}(z)$ [28], we used the rational expansion method introduced by Weideman [40].

For a surface plasmon wave to occur, the resonance condition is:

$$\frac{2\pi}{\lambda} n_c \sin\theta = \text{Re} \left[\frac{2\pi}{\lambda} \left(\frac{\epsilon_m n_s^2}{\epsilon_m + n_s^2} \right)^{1/2} \right] \tag{6}$$

where n_c , n_s , and ϵ_m are the fiber core refractive index, sensing layer refractive index, and metal layer dielectric constant, respectively [41]. For wavelength interrogation fiber optic SPR sensor, the condition is met at a specific wavelength (resonance wavelength), at which the intensity of the transmitted light is the lowest [42]. The resonance wavelength can be obtained from the SPR curve, which shows the detected

Fig. 2 **a** Real part of Au dielectric function using Drude, L-D, and B-B models compared with the measured data. **b** Imaginary part of Au dielectric function using Drude, L-D, and B-B models compared with the measured data

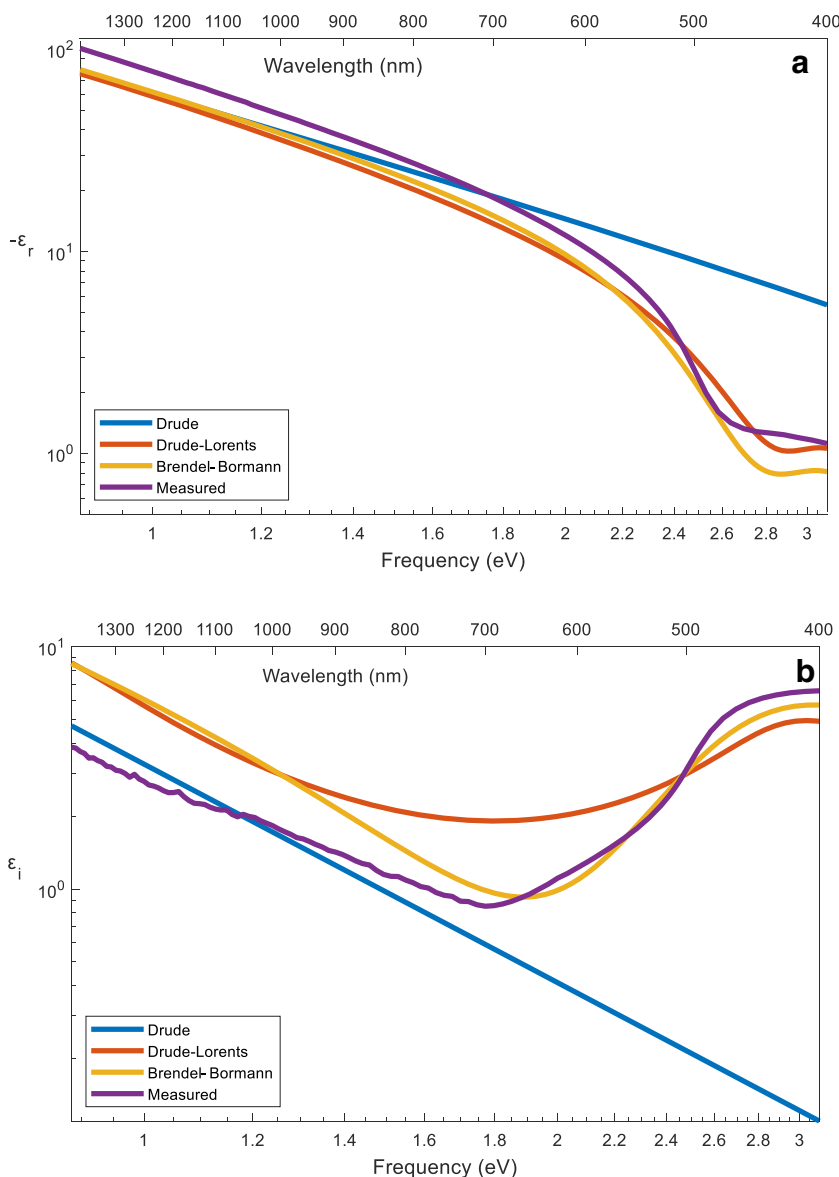
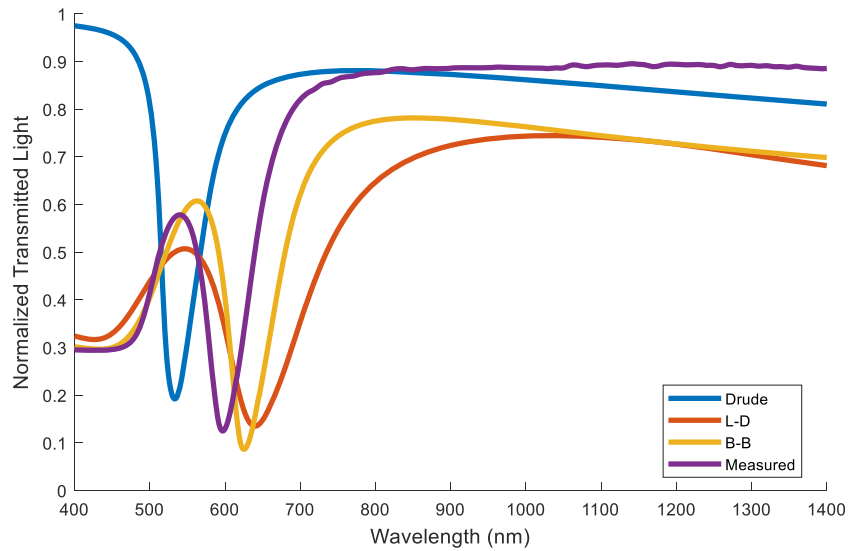


Fig. 3 Fiber optic SPR sensor normalized transmitted p-polarized light of Drude, L-D, and B-B models’ sensors compared with the measured dielectric function model’s sensor at RI 1.33



transmitted light at the fiber’s end, after passing through the sensing area, as a function of the wavelength.

The light was launched into the fiber from a collimated light source through a microscopic lens. For a given incidence angle θ , and a fiber core refractive index n_c , the corresponding optical power $P(\theta)$ is [43]:

$$P(\theta) \propto \frac{n_c^2 \sin\theta \cos\theta}{(1 - n_c^2 \cos^2\theta)^2} \tag{7}$$

To calculate the transmitted power, the reflection intensity coefficient (R_p) of each ray is raised to the power of its corresponding number of reflections (N_{ref}). Accordingly, the formula of the normalized transmitted power (P_t) for a p-polarized light is [44]:

$$P_t = \frac{\int_{\theta_{cr}}^{\pi/2} R_p^{N_{ref}(\theta)} P(\theta) d\theta}{\int_{\theta_{cr}}^{\pi/2} P(\theta) d\theta} \tag{8}$$

where R_p is the reflection intensity coefficient for a p-polarized incident wave and is defined by:

$$R_p = |r_p|^2 \tag{9}$$

Table 3 Error in sensor’s resonance wavelengths obtained using the three dielectric function models with reference to the one obtained using the measured dielectric function’s model at RI of 1.33

Model	Error %
Drude	10.72%
L-D	7.03%
B-B	4.69%

r_p represents the reflection coefficient for p-polarized light and was obtained by applying the N-layer model [45] and creating our 3-layer transfer matrix as described in [44].

$N_{ref}(\theta)$ is the total number of reflections of the light in the sensing region and is defined by:

$$N_{ref}(\theta) = \frac{L}{D \tan(\theta)} \tag{10}$$

where L is the length of the sensing area, D is the fiber core diameter, and θ is the incidence angle.

θ_{cr} is the fiber’s critical angle and is described by:

$$\theta_{cr} = \sin^{-1}\left(\frac{n_{cl}}{n_1}\right) \tag{11}$$

n_1 and n_{cl} are the refractive indices of the core and cladding, respectively.

Results

First, we calculated the Au dielectric function over our frequency range of interest from 0.8 to three (eV), i.e., wavelength range from 1400 down to 400 (nm) using Drude, L-D, and B-B models. The real and imaginary parts of the models-obtained dielectric functions compared to the measured data were illustrated in Fig. 2b.

As we can see from Fig. 2, the B-B model gives the best fit of the measured Au dielectric function in both its real and imaginary parts. On the contrary, Drude model has the worst fit of the three models. In spite of having the best fit for lower frequencies, its deviation increases rapidly above 1.8 eV (eV), i.e., under 688 nm especially for the imaginary part. This matched the previously reported results in [3, 28, 29, 31].

Table 4 Resonance wavelength (λ_{res}) values for each of the models through the RI range from 1.33 to 1.41

RI		1.33	1.34	1.35	1.36	1.37	1.38	1.39	1.40	1.41
Resonance wavelength	Drude	533	560	592	630	678	739	823	953	1212
	L-D	639	658	681	710	746	795	864	974	1218
	B-B	625	642	664	691	726	774	843	953	1176
	Measured	597	612	630	653	683	723	782	877	1029

Then, we calculated the SPR curve for the visible and near-infrared (NIR) range at a medium refractive index (RI) of 1.33, using each of the discussed dielectric function models' sensors and the measured dielectric function's sensor as shown in Fig. 3.

As we can see from Fig. 3, the SPR curve of the measured dielectric function sensor has its resonance wavelength at 597 nm. The nearest to it is the B-B model's curve at 625 nm, while the L-D model's is a bit higher than the B-B's at 639 nm. Moreover, the Drude's is the farthest at 533 nm. Note that Drude model SPR curve nearly matches the measured dielectric function above 700 nm and deviates under that as expected.

To evaluate the percentage relative error in determining the sensor's resonance wavelength using the three models with reference to the sensor's resonance wavelength using the measured dielectric function, we used Eq. (12):

$$\%Error = \left| \frac{Theoretical\ value - Measured\ value}{Measured\ value} \right| \times 100 \quad (12)$$

As we can see from Table 3, the Drude model's sensor has the highest error regarding the resonance wavelength at a refractive index of 1.33 compared with L-D model's which has lower error and B-B model's which is the nearest to the measured dielectric function model's value. The resonance wavelength (λ_{res}) values for each of the models through the RI range from 1.33 to 1.41 is indicated in Table 4.

From Table 4, it is worth noting that, while the resonance wavelength values of L-D and B-B models are always higher than that of the measured dielectric function's model, the Drude model's values are lower than that of the measured dielectric function's model only at the beginning of the RI range up to 1.37. From 1.38 up to 1.41, the Drude model's resonance wavelength becomes higher than that of the measured dielectric function's model.

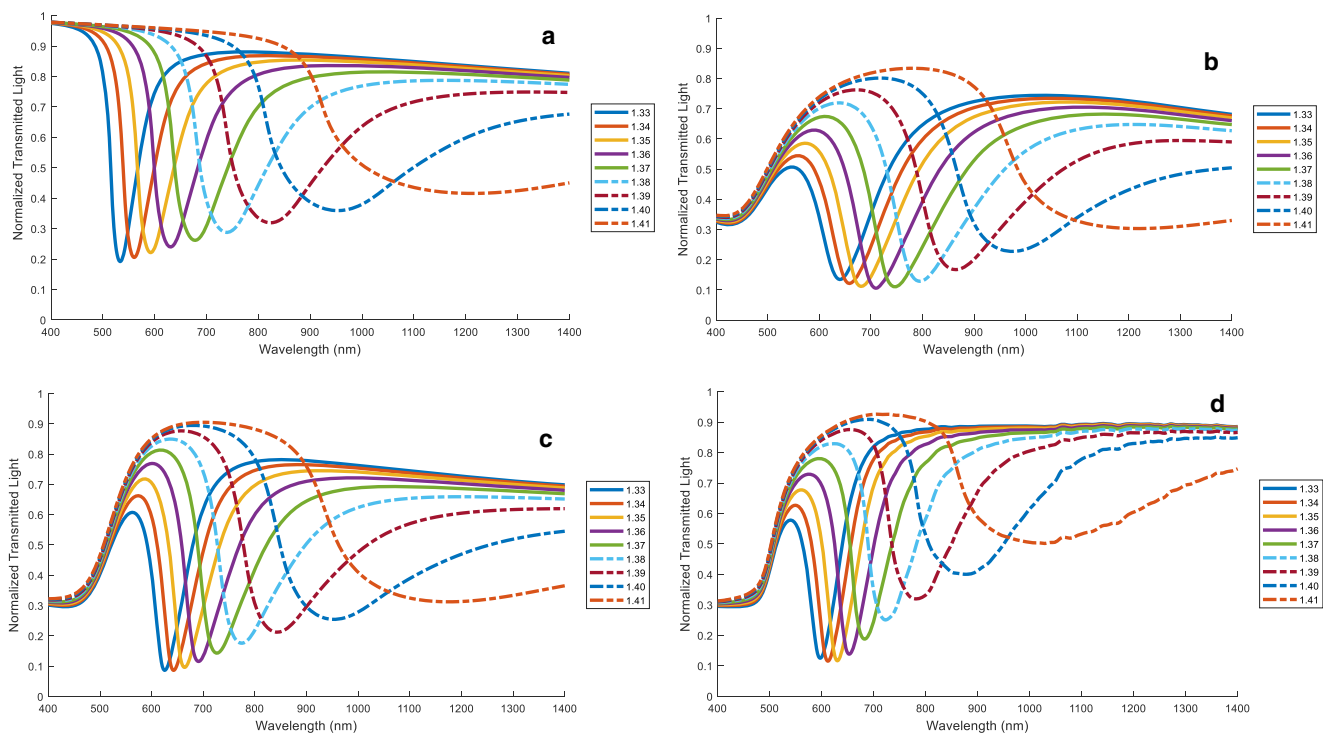


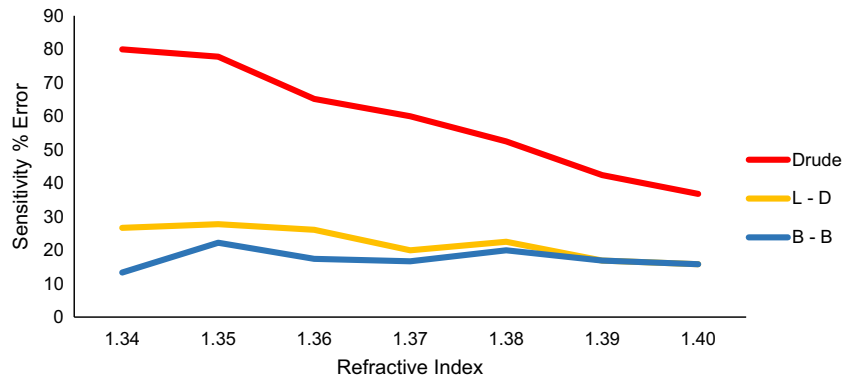
Fig. 4 **a** Normalized transmitted p-polarized light of Drude model's sensor for RI from 1.33 to 1.41. **b** Normalized transmitted p-polarized light of L-D model's sensor for RI from 1.33 to 1.41. **c** Normalized transmitted

p-polarized light of B-B model's sensor for RI from 1.33 to 1.41. **d** Normalized transmitted p-polarized light of the measured dielectric function model's sensor for RI from 1.33 to 1.41

Table 5 SPR sensor’s sensitivity using the three models and the measured dielectric function

RI		1.34	1.35	1.36	1.37	1.38	1.39	1.40
Sensitivity (μm/RIU)	Drude	2.7	3.2	3.8	4.8	6.1	8.4	13
	L-D	1.9	2.3	2.9	3.6	4.9	6.9	11
	B-B	1.7	2.2	2.7	3.5	4.8	6.9	11
	Measured	1.5	1.8	2.3	3	4	5.9	9.5

Fig. 5 Percentage relative error in sensitivity of SPR sensor using the three models with reference to the sensor’s sensitivity using the measured dielectric function’s model



We calculated the SPR curves for refractive indices from 1.33 to 1.41 for the discussed dielectric function models’ sensors and the measured dielectric function model’s sensor as shown in Fig. 4b, c, and d.

Figure 4b, c, and d show the difference in the obtained SPR curves using the three models’ sensors and the measured dielectric function’s model. At 400 nm, the normalized transmitted power equals 0.3 for the measured dielectric function’s model and B-B model. L-D’s value is between 0.3 and 0.4, and Drude’s value equals almost one. The minimum power level over the RI range is around 0.2 for Drude model; on the contrary, it reached 0.1 for the other models. For the higher frequencies, while L-D and B-B models power level stayed under 0.8, Drude model and the measured dielectric function’s model reached higher level around 0.9. We can also see that the Drude and the measured dielectric function models’ SPR curves have narrower dips than the other two models, especially the L-D model, which has the widest dips.

As the sensitivity of a sensor is its prominent feature, we calculated the sensitivity of each model’s sensor for the different RI values as shown in Table 5. The sensitivity of an SPR sensor with spectral interrogation equals the shift in the

resonance wavelength per unit change in the medium’s refractive index and is given by:

$$S_n(\mu\text{m}/\text{RIU}) = \frac{\delta\lambda_{res}}{\delta n_s} \tag{13}$$

where RIU is the refractive index unit [46]. The calculated sensitivity values of each sensor model over the RI range from 1.34 to 1.4 are indicated in Table 5.

As we can see from Table 5, the measured dielectric function’s sensor has the lowest sensitivity values for all the refractive indices. The sensitivity values of B-B model’s sensor are the closest to the measured dielectric function model’s and Drude’s are the furthest while L-D’s are in between and close to the B-B model’s having the same sensitivity values for RI values 1.39 and 1.40. The percentage relative error in sensitivity values of each model’s sensor and the measured dielectric function’s sensor as a reference is calculated and illustrated in Fig. 5.

As we can see from Fig. 5, the error in sensitivity calculation for Drude model’s sensor reached up to 80% between 1.33 and 1.34 RI with a mean relative error of 59.2%. As the RI reached higher values, the Drude model’s error gradually decreases. On the other hand, using B-B model greatly

Table 6 FWHM of the sensor’s SPR curves using the three models and the measured dielectric function

RI		1.33	1.34	1.35	1.36	1.37	1.38	1.39	1.40
FWHM (nm)	Drude	57	65	77	93	114	145	193	275
	L-D	90	100	111	126	148	164	190	237
	B-B	58	66	78	90	106	131	176	246
	Measured	51	54	59	64	78	102	147	220

Fig. 6 Percentage relative error in FWHM of SPR sensor curves using the three models with reference to the measured dielectric function’s model

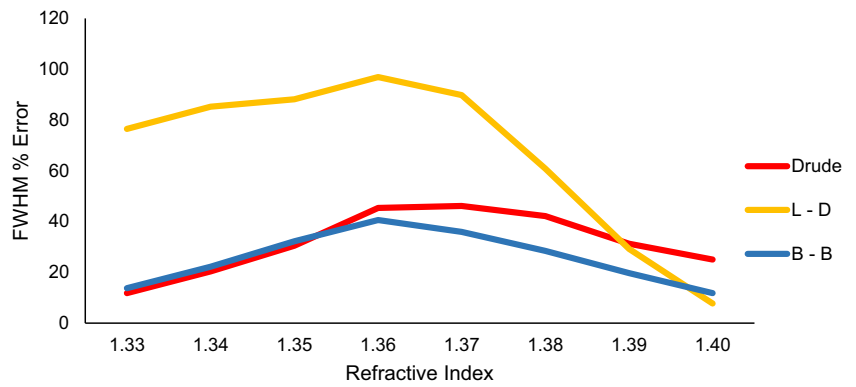


Table 7 SNR values of each sensor model for RI range from 1.33 to 1.4

RI		1.33	1.34	1.35	1.36	1.37	1.38	1.39	1.40
SNR	Drude	0.474	0.492	0.494	0.516	0.535	0.579	0.674	0.942
	L-D	0.211	0.230	0.261	0.286	0.331	0.421	0.579	1.030
	B-B	0.293	0.333	0.346	0.389	0.453	0.527	0.625	0.907
	Measured	0.294	0.333	0.390	0.469	0.513	0.578	0.646	0.691

decreased the relative error to a maximum of 22% between 1.34 and 1.35 RI, which is four times less than Drude model’s max error and almost constant through the entire RI range with a mean relative error of 17.4%. L-D model gives higher error than B-B model but still lower than Drude model’s error with a maximum of 27.8% between 1.34 and 1.35 RI and a mean of 22.3%.

The second investigated sensor parameter is the FWHM, which is defined as the spectral width of the sensor’s SPR curve at half maximum [47]. The lower the SPR curve spectral width the better, because it will be easier to distinguish smaller wavelength shifts. The values of FWHM of each sensor model for RI range from 1.33 to 1.4 are indicated in Table 6.

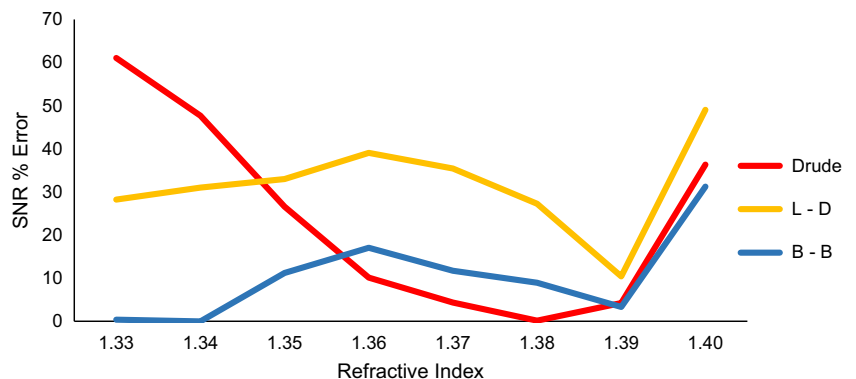
As we can see from Table 6, the measured dielectric function model has the lowest FWHM values over the entire range, and all the other models have a relatively higher FWHM values. Figure 6 depicts the percentage relative error in

FWHM values of each model’s sensor and the measured dielectric function model’s sensor as a reference.

Figure 6 indicates that Drude model unexpectedly gives better performance in terms of FWHM calculation accuracy than the other two models with respect to the measured dielectric function model’s values over the RI range from 1.33 to 1.35 with a max relative error of 46.2% at 1.37 RI and a mean relative error of 31.6%. B-B model’s performance is not as good as Drude’s, but not far from it, and precedes it above 1.36 with a max relative error of 40.6% at 1.36 RI and a mean relative error of 25.6%. L-D model is the least accurate among the three models with a max relative error of 96.9% at 1.36 RI and a mean relative error of 66.8%. It beats the other two models only at 1.4 RI.

The SNR of an SPR sensor is another important aspect; it indicates how accurately and precisely the resonance wavelength can be detected and, hence, the refractive index of the

Fig. 7 Percentage relative error in SNR of SPR sensor models with reference to the measured dielectric function’s model



sensing layer. For a spectral interrogation SPR sensor, the SNR is a dimensionless parameter defined by:

$$SNR = \frac{\delta\lambda_{res}}{FWHM} \quad (14)$$

where $\delta\lambda_{res}$ is the shift in the resonance wavelength of the SPR curve induced by an amount of change in the sensed medium refractive index [47]. The SNR values of each sensor model for RI range from 1.33 to 1.4 are stated in Table 7.

In Table 7, the Drude model's SNR values are always higher than that of the measured dielectric function's model. On the other hand, L-D and B-B models give lower SNR values than that of the measured dielectric function's model for all the RI range except at 1.4 RI. The percentage relative error in SNR values of each model's sensor and the measured dielectric function model's sensor as a reference was calculated and illustrated in Fig. 7.

From Fig. 7, it is obvious that B-B model gives very accurate SNR values with almost zero error from 1.33 to 1.34 RI, a max relative error of 31.2% at 1.4 RI, and a mean relative error of 10.5%. Drude model has a very high error at the start of RI range with a max of 61.1% at 1.33 RI and a mean relative error of 23.8%. The error decreases gradually as the RI increases until it becomes the dominant model in terms of accuracy from 1.36 up to 1.39 RI. L-D model has an intermediate relative error from 1.33 to 1.34 RI and gives the highest error among the three models over the rest of the RI range with a max of 49% at 1.4 RI and a mean relative error of 31.7%.

Discussion and Conclusion

In this paper, at first we confirmed that Brendel-Bormann model gives the most accurate representation of Au dielectric function among the three most used dielectric function models (Drude, Lorentz-Drude, and Brendel-Bormann) compared with the Au measured dielectric function in the visible and NIR range.

Then, we investigated the performance of each of the three models along with the measured data as a reference, when adopted in an SPR sensor model. Based on our results, Brendel-Bormann model preceded the other two models in determining the SPR sensor's main parameters, sensitivity, FWHM, and SNR with a mean relative error of 17.5%, 25.6%, and 10.5%, respectively. Drude model gave the second best result for FWHM and SNR with a mean relative error of 31.6% and 23.8%, respectively, and the least accurate sensitivity values with a mean relative error of 59.2%. L-D model performed better than Drude model in case of sensitivity with a mean relative error of 22.3% but was the least accurate in determining FWHM and SNR with a mean relative error of 66.8% and 31.7%, respectively.

Using Drude model to describe the gold complex dielectric function of an SPR sensor severely degrades the accuracy of the sensor's sensitivity and FWHM and SNR calculations. Using L-D model instead of Drude's improves the accuracy of the sensitivity calculation but degrades the FWHM and SNR calculation accuracy. The best choice is B-B model, which has the best accuracy for all the sensor's parameter calculations leading to a more realistic representation of the SPR sensor and reducing the gap between theoretical sensor's models and the experimental results.

References

- Kretschmann E, Raether H (1968) Notizen: Radiative decay of non radiative surface plasmons excited by light. *Z Naturforsch A* 23. <https://doi.org/10.1515/zna-1968-1247>
- Otto A (1968) Excitation of nonradiative surface plasma waves in silver by the method of frustrated total reflection. *Zeitschrift für Physik A Hadrons and nuclei* 216(4):398–410. <https://doi.org/10.1007/BF01391532>
- Nickelson L (2019) *Electromagnetic theory and plasmonics for engineers*. Springer Singapore, Singapore
- Homola J (2008) Surface plasmon resonance sensors for detection of chemical and biological species. *Chem Rev* 108(2):462–493. <https://doi.org/10.1021/cr068107d>
- Roh S, Chung T, Lee B (2011) Overview of the characteristics of micro- and nano-structured surface plasmon resonance sensors. *Sensors (Basel)* 11(2):1565–1588. <https://doi.org/10.3390/s110201565>
- Wood RW (1902) XLII. On a remarkable case of uneven distribution of light in a diffraction grating spectrum. *The London, Edinburgh, and Dublin Philosophical Magazine and Journal of Science* 4(21):396–402. <https://doi.org/10.1080/14786440209462857>
- Liedberg B, Nylander C, Lunström I (1983) Surface plasmon resonance for gas detection and biosensing. *Sensors Actuators* 4:299–304. [https://doi.org/10.1016/0250-6874\(83\)85036-7](https://doi.org/10.1016/0250-6874(83)85036-7)
- Melo AAd, Silva TBd, Santiago MFdS, Moreira CdS, Cruz RMS (2019) Theoretical analysis of sensitivity enhancement by graphene usage in optical fiber surface plasmon resonance sensors. *IEEE Trans Instrum Meas* 68(5):1554–1560. <https://doi.org/10.1109/TIM.2018.2882148>
- Rithesh Raj D, Prasanth S, Vineeshkumar TV, Sudarsanakumar C (2016) Surface plasmon resonance based fiber optic dopamine sensor using green synthesized silver nanoparticles. *Sensors Actuators B Chem* 224:600–606. <https://doi.org/10.1016/j.snb.2015.10.106>
- Zhao J, Cao S, Liao C, Wang Y, Wang G, Xu X, Fu C, Xu G, Lian J, Wang Y (2016) Surface plasmon resonance refractive sensor based on silver-coated side-polished fiber. *Sensors Actuators B Chem* 230:206–211. <https://doi.org/10.1016/j.snb.2016.02.020>
- Semwal V, Gupta BD (2019) Experimental studies on the sensitivity of the propagating and localized surface plasmon resonance-based tapered fiber optic refractive index sensors. *Appl Opt* 58(15):4149–4156. <https://doi.org/10.1364/AO.58.004149>
- Goswami N, Chauhan KK, Saha A (2016) Analysis of surface plasmon resonance based bimetal coated tapered fiber optic sensor with enhanced sensitivity through radially polarized light. *Opt Commun* 379:6–12. <https://doi.org/10.1016/j.optcom.2016.05.047>
- Jiang S, Li Z, Zhang C, Gao S, Li Z, Qiu H, Li C, Yang C, Liu M, Liu Y (2017) A novel U-bent plastic optical fibre local surface

- plasmon resonance sensor based on a graphene and silver nanoparticle hybrid structure. *J Phys D Appl Phys* 50(16):165105. <https://doi.org/10.1088/1361-6463/aa628c>
14. Arcas ADS, Dutra FDS, Allil RCSB, Werneck MM (2018) Surface plasmon resonance and bending loss-based U-shaped plastic optical fiber biosensors. *Sensors* 18(2):648. <https://doi.org/10.3390/s18020648>
 15. Zhang C, Li Z, Jiang SZ, Li CH, Xu SC, Yu J, Li Z, Wang MH, Liu AH, Man BY (2017) U-bent fiber optic SPR sensor based on graphene/AgNPs. *Sensors Actuators B Chem* 251:127–133. <https://doi.org/10.1016/j.snb.2017.05.045>
 16. Arasu PT, Noor ASM, Shabaneh AA, Yaacob MH, Lim HN, Mahdi MA (2016) Fiber Bragg grating assisted surface plasmon resonance sensor with graphene oxide sensing layer. *Opt Commun* 380:260–266. <https://doi.org/10.1016/j.optcom.2016.05.081>
 17. Zhang X, Chen J, González-Vila Á, Liu F, Liu Y, Li K, Guo T (2019) Twist sensor based on surface plasmon resonance excitation using two spectral combs in one tilted fiber Bragg grating. *J Opt Soc Am B* 36(5):1176–1182. <https://doi.org/10.1364/JOSAB.36.001176>
 18. Baiad MD, Kashyap R (2015) Concatenation of surface plasmon resonance sensors in a single optical fiber using tilted fiber Bragg gratings. *Opt Lett* 40(1):115–118. <https://doi.org/10.1364/OL.40.000115>
 19. Li W, Ren K, Zhou J (2016) Aluminum-based localized surface plasmon resonance for biosensing. *TrAC Trends Anal Chem* 80:486–494. <https://doi.org/10.1016/j.trac.2015.08.013>
 20. Tanabe I, Tanaka YY, Watari K, Hanulia T, Goto T, Inami W, Kawata Y, Ozaki Y (2017) Far- and deep-ultraviolet surface plasmon resonance sensors working in aqueous solutions using aluminum thin films. *Sci Rep* 7(1):5934. <https://doi.org/10.1038/s41598-017-06403-9>
 21. Xu H, Wu L, Dai X, Gao Y, Xiang Y (2016) An ultra-high sensitivity surface plasmon resonance sensor based on graphene-aluminum-graphene sandwich-like structure. *J Appl Phys* 120(5):053101. <https://doi.org/10.1063/1.4959982>
 22. Mishra SK, Zou B, Chiang KS (2016) Surface-plasmon-resonance refractive-index sensor with cu-coated polymer waveguide. *IEEE Photon Technol Lett* 28(17):1835–1838. <https://doi.org/10.1109/LPT.2016.2573322>
 23. Rifat AA, Mahdiraji GA, Ahmed R, Chow DM, Sua YM, Shee YG, Adikan FRM (2016) Copper-graphene-based photonic crystal fiber plasmonic biosensor. *IEEE Photonics Journal* 8(1):1–8. <https://doi.org/10.1109/JPHOT.2015.2510632>
 24. Shah K, Sharma NK, Sajal V (2018) Analysis of fiber optic SPR sensor utilizing platinum based nanocomposites. *Opt Quant Electron* 50(6):265. <https://doi.org/10.1007/s11082-018-1533-x>
 25. Shah K, Sharma NK, Sajal V (2018) Simulation of LSPR based fiber optic sensor utilizing layer of platinum nanoparticles. *Optik* 154:530–537. <https://doi.org/10.1016/j.ijleo.2017.10.062>
 26. Zhou X, Yu Q, Peng W (2019) Mid-infrared surface plasmon resonance sensor based on silicon-doped InAs film and chalcogenide glass fiber. *Opt Laser Technol* 120:105686. <https://doi.org/10.1016/j.optlastec.2019.105686>
 27. Wang R, Li T, Shao X, Li X, Gong H (2015) The simulation of localized surface plasmon and surface plasmon polariton in wire grid polarizer integrated on InP substrate for InGaAs sensor. *AIP Adv* 5(7):077128. <https://doi.org/10.1063/1.4926842>
 28. Rakić AD, Djurišić AB, Elazar JM, Majewski ML (1998) Optical properties of metallic films for vertical-cavity optoelectronic devices. *Appl Opt* 37(22):5271–5283. <https://doi.org/10.1364/AO.37.005271>
 29. Jahanshahi P, Ghomeishi M, Adikan F (2014) Study on dielectric function models for surface plasmon resonance structure. *TheScientificWorldJournal* 2014:503749–503746. <https://doi.org/10.1155/2014/503749>
 30. Mirzaei Y, Rostami G, Dolatyari M, Rostami A (2015) Investigation of efficient mathematical permittivity modeling for modal analysis of plasmonics layered structures. *Optik* 126(3):323–327. <https://doi.org/10.1016/j.ijleo.2014.08.175>
 31. Derkachova A, Kolwas K, Demchenko I (2016) Dielectric function for gold in plasmonics applications: size dependence of plasmon resonance frequencies and damping rates for nanospheres. *Plasmonics* 11(3):941–951. <https://doi.org/10.1007/s11468-015-0128-7>
 32. Shukla S, Sharma NK, Sajal V (2015) Sensitivity enhancement of a surface plasmon resonance based fiber optic sensor using ZnO thin film: a theoretical study. *Sensors Actuators B Chem* 206:463–470. <https://doi.org/10.1016/j.snb.2014.09.083>
 33. Luan N, Wang R, Lv W, Yao J (2015) Surface plasmon resonance sensor based on D-shaped microstructured optical fiber with hollow core. *Opt Express* 23(7):8576–8582. <https://doi.org/10.1364/OE.23.008576>
 34. Feng X, Yang M, Luo Y, Tang J, Guan H, Fang J, Lu H, Yu J, Zhang J, Chen Z (2017) Long range surface plasmon resonance sensor based on side polished fiber with the buffer layer of magnesium fluoride. *Opt Quant Electron* 49(4):147. <https://doi.org/10.1007/s11082-017-0955-1>
 35. Kumar S, Yadav GC, Sharma G, Singh V (2018) Study of surface plasmon resonance sensors based on silver–gold nanostructure alloy film coated tapered optical fibers. *Applied Physics A* 124(10):695. <https://doi.org/10.1007/s00339-018-2120-5>
 36. Wei W, Nong J, Tang L, Wang N, Chuang C-J, Huang Y (2017) Graphene-MoS₂ hybrid structure enhanced fiber optic surface plasmon resonance sensor. *Plasmonics* 12(4):1205–1212. <https://doi.org/10.1007/s11468-016-0377-0>
 37. Sakib MN, Hossain MB, Al-tabatabaie KF, Mehedi IM, Hasan MT, Hossain MA, Amiri IS (2019) High performance dual core D-shape PCF-SPR sensor modeling employing gold coat. *Results in Physics* 15:102788. <https://doi.org/10.1016/j.rinp.2019.102788>
 38. McPeak KM, Jayanti SV, Kress SJP, Meyer S, Iotti S, Rossinelli A, Norris DJ (2015) Plasmonic films can easily be better: rules and recipes. *ACS Photonics* 2(3):326–333. <https://doi.org/10.1021/ph5004237>
 39. Huynh TL, Binh LN MECSE-10-2004 Fibre design for dispersion compensation and raman amplification. In: 2004
 40. Weideman JAC (1994) Computation of the complex error function. *SIAM J Numer Anal* 31(5):1497–1518
 41. Sharma AK, Gupta BD (2007) On the performance of different bimetallic combinations in surface plasmon resonance based fiber optic sensors. *J Appl Phys* 101(9):093111. <https://doi.org/10.1063/1.2721779>
 42. Gupta B, Verma RK (2009) Surface plasmon resonance-based fiber optic sensors: principle, probe designs, and some applications. *Journal of Sensors* 2009:1–12. <https://doi.org/10.1155/2009/979761>
 43. Gupta B, Sharma A, Singh CD (1993) Evanescent wave absorption sensors based on uniform and tapered fibres. A comparative study of their sensitivities. *Int J Optoelectron* 8:409–418
 44. Gupta B, Sharma A (2005) Sensitivity evaluation of a multi-layered surface plasmon resonance-based fiber optic sensor: a theoretical study. *Sensors Actuators B Chem* 107:40–46. <https://doi.org/10.1016/j.snb.2004.08.030>
 45. Abelès F (1950) Recherches sur la propagation des ondes électromagnétiques sinusoidales dans les milieux stratifiés. *Ann Phys* 12(5):596–640
 46. Homola J (1997) On the sensitivity of surface plasmon resonance sensors with spectral interrogation. *Sensors Actuators B Chem* 41(1):207–211. [https://doi.org/10.1016/S0925-4005\(97\)80297-3](https://doi.org/10.1016/S0925-4005(97)80297-3)
 47. Cennamo N, Zeni L (2014) Bio and chemical sensors based on surface plasmon resonance in a plastic optical fiber. In: <https://doi.org/10.5772/57148>